CONDENSED MATTER PHYSICS

High-temperature surface state in Kondo insulator $U_3Bi_4Ni_3$

Christopher Broyles[1], Xiaohan Wan[2], Wenting Cheng[2], Dingsong Wu[3], Hengxin Tan[4], Qiaozhi Xu[1], Shannon L. Gould[1], Hasan Siddiquee[1], Leyan Xiao[1], Ryan Chen[1], Wanyue Lin[1], Yuchen Wu[1], Prakash Regmi[5], Yun Suk Eo[5], Jieyi Liu[6], Yulin Chen[3,7], Binghai Yan[4]*, Kai Sun[2]*, Sheng Ran[1]*

The resurgence of interest in Kondo insulators has been driven by two major mysteries: the presence of metallic surface states and the observation of quantum oscillations. To further explore these mysteries, it is crucial to investigate another similar system beyond the two existing ones, SmB_6 and YbB_{12}. Here, we address this by reporting on a Kondo insulator, $U_3Bi_4Ni_3$. Our transport measurements reveal that a surface state emerges below 250 kelvin and dominates transport properties below 150 kelvin, which is well above the temperature scale of SmB_6 and YbB_{12}. At low temperatures, the surface conductivity is about one order of magnitude higher than the bulk. The robustness of the surface state indicates that it is inherently protected. The similarities and differences between $U_3Bi_4Ni_3$ and the other two Kondo insulators will provide valuable insights into the nature of metallic surface states in Kondo insulators and their interplay with strong electron correlations.

INTRODUCTION

In Kondo lattice materials, interactions between conduction electrons and localized *f* electrons lead to the screening of localized magnetic moments, generating a spin-scattering resonance state and a hybridization gap (*1*–*5*). If the Fermi energy lies within the hybridization gap, the system is a Kondo insulator (*6*). Two well-known examples are SmB_6 and YbB_{12}, both of which exhibit a curious phenomenon: the saturation of electrical resistivity at low temperatures (*7*, *8*). This resistivity saturation is particularly well-documented in SmB_6 and has been the focus of extensive study for decades due to the mystery it presents (*9*). In a conventional insulator, resistivity should increase as temperature decreases, but in these materials, it unexpectedly plateaus, indicating an unusual form of conduction. Various theories, such as impurity states or in-gap states, have been proposed to explain this behavior (*10*–*12*). In the past decade, a hypothesis has emerged suggesting that the resistivity saturation in SmB_6, and potentially in YbB_{12}, might be due to the presence of metallic surface states of topological origin (*13*–*18*). This idea has sparked substantial interest and is supported by numerous experimental studies, although some results show inconsistencies with a purely topological interpretation (*19*–*22*). The exact cause of the resistivity saturation and the full nature of the surface states in SmB_6 and YbB_{12} remain subjects of active investigation.

In addition to the mystery of resistivity saturation, both SmB_6 and YbB_{12} exhibit another intriguing phenomenon: the observation of quantum oscillations (*23*–*30*). Typically, quantum oscillations are associated with a Fermi surface in metals, making their presence in these insulating materials particularly unexpected. These oscillations suggest that SmB_6 and YbB_{12} might host unconventional excitations, such as neutral fermions or other exotic states (*23*, *24*, *26*, *27*), that challenge the theoretical understanding of a Kondo insulating state (*31*–*39*). While metallic surface states have been proposed as a possible explanation, they do not fully account for the quantum oscillations, as these oscillations appear to originate from the bulk of the material. Nevertheless, the fact that both SmB_6 and YbB_{12} exhibit both resistivity saturation and quantum oscillations suggests that these two phenomena may be related in some way, even if the underlying mechanisms are different.

Given the unresolved mysteries surrounding SmB_6 and YbB_{12}, discovering another Kondo insulator that exhibits similar phenomena at a different energy scale would be invaluable. Uranium-based Kondo lattice systems present a promising platform for such discoveries, as the stronger hybridization between U 5*f* electrons and conduction electrons can result in a considerably higher hybridization gap and Kondo temperature compared to their rare-earth counterparts (*40*–*42*). To this end, we identified a potential candidate: $U_3Bi_4Ni_3$. It crystallizes onto a cubic lattice with noncentrosymmetric symmetry in the space group I-43d (no. 220) (*43*), isostructual to the Ce-based Kondo insulator $Ce_3Bi_4Pt_3$ (Fig. 1A). Upon cooling below $T_K = 100$ K, there is a suppression of magnetic susceptibility (*43*) and an increase of correlation between 5*f* and conduction electrons (*44*), both are signatures of Kondo screening of the uranium local moments. The hybridization gap was measured using photoemission spectroscopy (*43*), revealing a gap of 72 meV, while nuclear quadrupole resonance (NQR) T_1^{-1} spin-lattice relaxation time measurements (*44*) found a smaller gap of 19 meV. In this work, we provide conclusive evidence of metallic surface state of $U_3Bi_4Ni_3$ that emerges below 250 K, dominating the transport properties below 150 K. This high-temperature, surface-dominated conduction in a Kondo insulator is unprecedented and could consequentially advance our understanding of the fundamental physics underlying metallic surface states in strongly correlated systems.

RESULTS

Kondo insulating ground state

First, we characterize the Kondo insulator behavior of $U_3Bi_4Ni_3$. At high temperatures, the magnetic susceptibility, M/H, shows a

[1]Department of Physics, Washington University in St. Louis, St. Louis, MO 63130, USA. [2]Department of Physics, University of Michigan, Ann Arbor, MI 48109, USA. [3]Department of Physics, University of Oxford, Oxford OX1 3PU, UK. [4]Department of Condensed Matter Physics, Weizmann Institute of Science, Rehovot 7610001, Israel. [5]Department of Physics and Astronomy, Texas Tech University, Lubbock, TX 79409, USA. [6]Diamond Light Source, Didcot OX11 0DE, UK. [7]ShanghaiTech Laboratory for Topological Physics, Shanghai 200031, People's Republic of China.
*Corresponding author. Email: binghai.yan@weizmann.ac.il (B.Y.); sunkai@umich.edu (K.S.); rans@wustl.edu (S.R.)

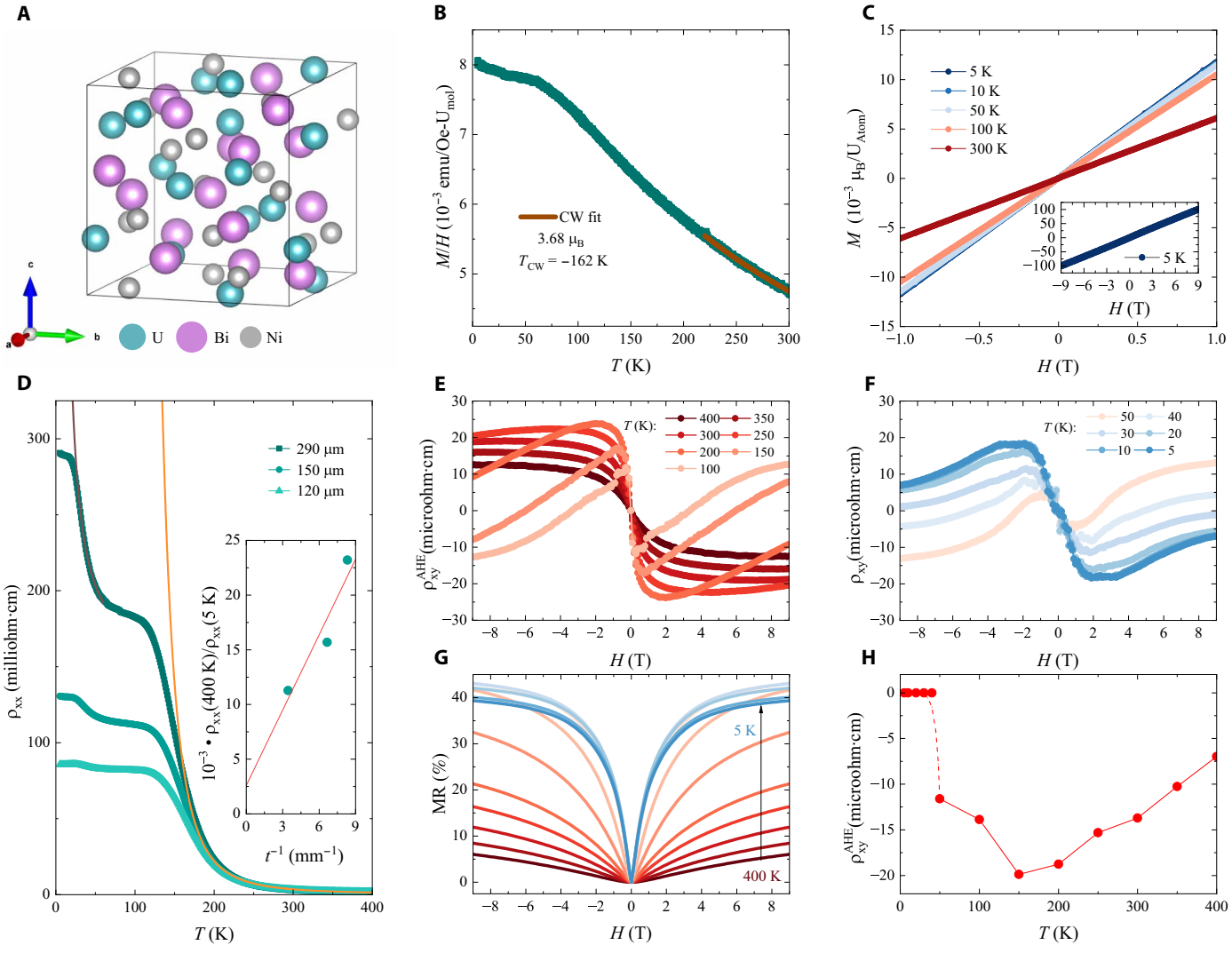

Fig. 1. Bulk Kondo insulator characterization. (**A**) The crystal structure of $U_3Bi_4Ni_3$, space group no. 220 (I-43d). (**B**) The magnetic susceptibility measured from room temperature down to 5 K, with a magnetic field of 0.1 T. (**C**) Magnetic field sweeps up to 1 T for various temperatures between 5 and 300 K. The inset displays a 9-T field sweep at 5 K. (**D**) The temperature dependence of ρ_{xx}, measured on a single crystal which was successively polished to thicknesses of 290, 150, and 120 μm, with a fitting applied above 200 K (orange, Δ = 95 meV) and between 30 and 60 K (brown, Δ = 1.5 meV). The inset displays ρ(400 K)/ρ(5 K) versys t^{-1}, modeled by the equation $\rho(400\,K)/\rho = (2\,\sigma_s/\sigma_{400\,K})\,t^{-1} + \sigma_b/\sigma_{400\,K}$. The linear fitting provides a slope of 2.3 ± 0.8 and an intercept of 3 ± 5*10 − 3. (**E** and **F**) The Hall resistivity (ρ_{xy}) field sweeps for $T \geq 100$ K are displayed in (E), while those for $T \leq 50$ K are shown in (F). (**G**) The magneto-resistance (MR) measured up to 9 T and presented for a variety of temperatures between 400 K and 5 K. (**H**) The anomalous Hall resistivity (ρ_{xy}^{AHE}), extracted from the two-band + *C* fittings (see the Supplementary Materials).

Curie-Weiss temperature dependence, fitting to a magnetic moment of 3.68 μ_B and $T_{CW} = -162$ K (Fig. 1B). Below 100 K, a signature of Kondo screening emerges, with M/H saturating to a value near $8 \cdot 10^{-3}$ emu / Oe - U_{mol}. This is consistent with a nuclear magnetic resonance/NQR study (*44*), which demonstrated a breakdown of the scaling between the Knight shift and magnetic susceptibility below 100 K. The field dependent magnetization, $M(H)$, reveals no ferromagnetic magnetic ordering or field-induced magnetic transition, with linear scaling for 5 K ≤ T ≤ 300 K (Fig. 1C).

The longitudinal resistivity (ρ_{xx}) resembles that of a narrow gap semiconductor at room temperature, with Δ = 95 meV (Fig. 1D). This gap size is appreciably larger than those observed in SmB_6 and YbB_{12} (*45*–*49*). As the temperature is lowered past the Kondo temperature ($T_K \approx 100$ K), ρ_{xx} flattens around 185 milliohm·cm, before an additional increase below 50 K, leading to a saturation at 290 milliohm·cm. An Arrhenius fit for 30 K ≤ T ≤ 60 K gives an activation gap of Δ = 1.5 meV. This temperature dependence could be consistent with Kondo hybridization renormalizing and reducing Δ below 100 K; however, the low-temperature saturation in ρ_{xx} is more than an order of magnitude larger than previously reported (*43*).

The magneto-transport measurements, displayed in Fig. 1 (E to G), provide further support of the Kondo coherent ground state. The high-temperature Hall resistivity (ρ_{xy}) exhibits a sigmoid-like shape, which cannot be accurately represented by a simple two-band model and is typically indicative of the anomalous Hall effect (*50*). The anomalous Hall is most clearly seen at 150 K, with a distinct, sharp

jump near zero magnetic field. By incorporating a constant into the two band Hall model (*51*), ρ_{xy}^{AHE} is extracted, and the temperature dependence is plotted in Fig. 1H. The anomalous Hall contribution gradually increases from room temperature to 150 K, after which it begins to decrease. This overall temperature dependence of the anomalous Hall effect is consistent with what has been observed in other Kondo lattice systems (*52*). Above the Kondo temperature, incoherent Kondo scattering dominates the transport properties. A modest magnetic field can polarize the local moments, leading to the anomalous Hall effect through a scattering mechanism (*52*, *53*). As the temperature decreases, a smaller magnetic field is needed to polarize the local moments; thus, the curve narrows and transitions into a sharp, step-like shape at 150 K. In the meantime, Kondo scattering logarithmically increases with the decreasing temperature, enhancing the anomalous Hall effect (*54*, *55*). Once Kondo scattering becomes coherent below T_K, the anomalous Hall gradually decreases. Note that below 50 K, the anomalous Hall contribution becomes negligible, and the Hall data fit equally well with a pure two-band model.

To further confirm the Kondo ground state of $U_3Bi_4Ni_3$, we performed angle-resolved photoemission spectroscopy (ARPES) measurements at $T = 20$ K. To highlight the spectral profile of U 5*f* character, we used 98-eV photon energy, which resonantly enhances the photoionization cross section of U 5*f* states. Figure 2 presents the energy spectra for the resonant condition at 98 eV and the off-resonant condition at 92 eV for comparison. While both spectra show a strong maximum at −2 eV, indicative of a flat band, the resonant enhanced band image maintains a strong intensity until E_F. The integrated energy distribution curve (EDC) reveals a refined structure near the Fermi level, with two peaks within 300 meV of E_F (indicated by red arrows). These weak peaks indicate U 5*f* multiplet states, which participate in the many-body Kondo resonance, as seen in other uranium-based Kondo lattice systems (*56*, *57*). The EDC of both 98 and 92 eV is suppressed at Fermi energy, indicating the insulating nature. The suppressed overall intensity at the Fermi level and the enhanced U 5*f* spectral weight near the Fermi energy in the resonant spectrum are consistent with a Kondo insulator, similar to observations in SmB_6 and YbB_{12} (*20*, *58*, *59*).

Metallic surface state

The temperature-dependent resistivity of $U_3Bi_4Ni_3$ exhibits a plateau below 150 K, shown in Fig. 1D. Similar plateaus have been observed in both SmB_6 (*7*) and YbB_{12} (*8*), indicative of either a metallic surface state or extended in-gap states. To identify the origin of the plateau, we performed a thickness-dependent study. The sample was successively polished to 150 and 120 μm. Above 200 K, the resistivity is essentially independent of thickness, which is a clear indication of bulk transport (Fig. 1D). In contrast, at low temperatures, the resistivity markedly decreases as the thickness is reduced. This reduction suggests that the resistance no longer scales linearly with thickness, a clear sign of surface charge transport.

To more accurately determine the bulk and surface transport coefficients, we use a nonlocal transport measurement, with the inverted resistance setup (*60*). The inverted transport measurement makes use of the Corbino disk geometry depicted in Fig. 3A, where electrode 2 acts as a two-dimensional Faraday cage for the surface area enclosed by this electrode. This technique has been reliably used to decouple the surface and the bulk conduction channels of SmB_6 and other strongly correlated insulators (*61*, *62*). Within this setup, we can measure two distinct four-terminal resistances: $R_{12;12}$ and $R_{12;34}$, where the first pair of indices denotes the current-carrying electrodes, and the second pair represents the voltage-measuring electrodes. For bulk-dominated transport, both $R_{12;12}$ and $R_{12;34}$ are proportional to the bulk resistivity. Conversely, in the scenario where surface transport dominates, $R_{12;12}$ and $R_{12;34}$ will show distinctly different dependencies on surface and bulk resistivity. This distinction arises because, when current is introduced between electrodes (1) and (2), charge carriers traverse parallel paths from $1 \rightarrow 2$ and $1 \rightarrow 3 \rightarrow 4 \rightarrow 2$, leveraging the enhanced conductivity of the surface. Therefore, in cases of surface-dominant transport, $R_{12;12}$ is directly proportional to the surface resistivity (i.e., $R_{12;12} \propto \rho_s$), while $R_{12;34}$ receives mixed contributions from both bulk and surface resistivity and exhibits a scaling behavior characterized by an inverse-gap dependence, (i.e., $R_{12;34} = Ct\frac{\rho_s^2}{\rho_b} \propto \mathrm{Exp}\left[-\frac{\Delta}{k_B T}\right]$) (*60*), where C is a constant, t is the sample thickness, ρ_s is the surface resistivity, ρ_b is the bulk resistivity, Δ is the energy gap, k_B is the Boltzmann

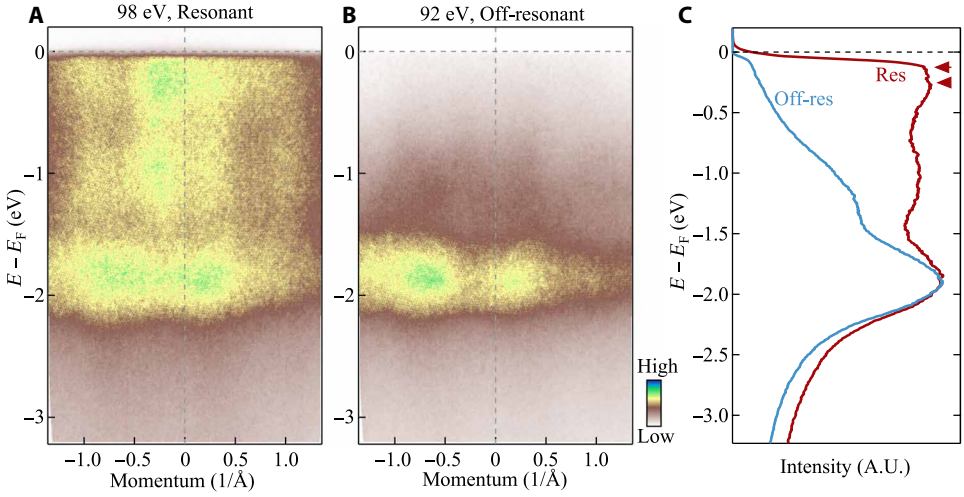

Fig. 2. Resonant enhanced ARPES. (**A**) The intensity map of energy versus angle for the resonant condition of 98 eV. (**B**) The off-resonant condition, with a photon energy of 92 eV. (**C**) The integrated EDC of the resonant and off-resonant conditions, demonstrating *f*-band weight near E_F. All data were taken at 6 K. A.U., arbitrary units.

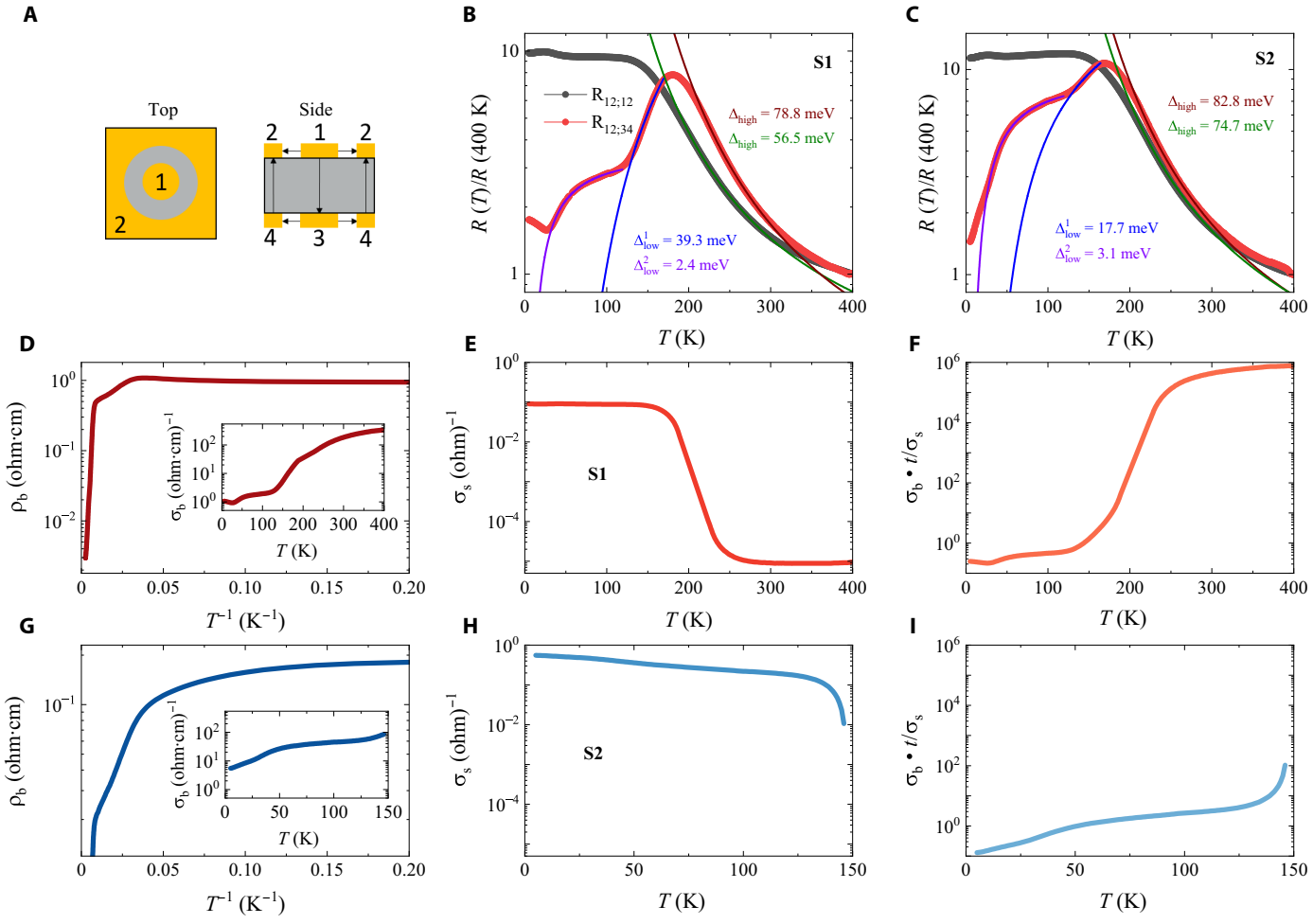

Fig. 3. Corbino disk and FEA. (**A**) The measurement geometry of the Corbino disk, shown from the top and cross-sectional side views. (**B** and **C**) Corbino disk samples 1 and 2 measured in the $R_{12;12}$ and $R_{12;34}$ configurations. (**D** and **E**) Using FEA to simulate the transport of S1, the bulk resistivity is plotted in (D), with the bulk conductivity in the inset, and the surface conductivity is displayed in (E). (**F**) The ratio of the bulk and surface conductivity, with $t = 210$ μm. (**G** to **I**) The FEA results for sample 2, with a thickness of 130 μm, presented below the surface state onset.

constant, and T is the temperature. The inverse-gap behavior is explained in more details in the Supplementary Materials.

Multiple $U_3Bi_4Ni_3$ samples were polished to a thickness ranging between 130 and 210 μm, and the Corbino disk electrodes were patterned on the top and bottom faces. Here, we present two Corbino disk samples in Fig. 3, which have been measured in the $R_{12;12}$ and $R_{12;34}$ configurations. The $R_{12;12}$ configuration has similar behavior to $\rho_{xx}(T)$ but only saturates at $R(5\text{K})/R(400\text{K}) \approx 10$ (Fig. 3, B and C). When measured in the $R_{12;34}$ configuration, the peak values reaches roughly 10 before the insulator-metal crossover. To compare the activated scaling, Arrhenius fittings were applied between 200 and 300 K, revealing a gap ranging from 78.8 to 82.8 meV and 56.5 to 74.7 meV for $R_{12;34}$ and $R_{12;12}$, respectively. Below the surface state onset, $R_{12;34}$ displays a dual inverse-gap behavior. The initial gap has values ranging from $\Delta^1_{low} = 17.7$ to 39.3 meV and transitions to a much smaller gap of $\Delta^2_{low} = 2.4$ to 3.1 meV. At low temperatures, sample 1 (S1) has a rise in $R_{12;34}$ around 25 K. The variety of these surface transport features demonstrates the robust nature of the surface state to carrier doping and impurities that characterize the sample variation.

The use of finite element analysis (FEA) allows the separation of the bulk and surface transport properties. We conducted simulations of the charge transport using a geometry that mirrors the experimental setup. By using the bulk resistivity (ρ_b) and surface conductivity (σ_s) as fitting parameters, we compare the simulated outcome with the experimental values of $R_{12;12}$ and $R_{12;34}$. This allowed us to extract the fitted values of ρ_b and σ_s at varying temperatures. The results of these fittings are displayed in Fig. 3 (D to I). The bulk resistivity of S1 is plotted versus T^{-1} in Fig. 3D, which shows an activation gap of 97.4 meV above 150 K and a much smaller activation gap of 3.2 meV below $T_K = 100$ K. As the temperature drops below 30 K, ρ_b saturates, likely due to the contribution of an impurity band or other in-gap state at low temperatures. The surface conductivity of S1 markedly increases from 250 K and exhibits nearly temperature-independent behavior below 150 K. The ratio of $\sigma_b{}^* t/\sigma_s$ reaches unity at 150 K, marking a crossover in the transport properties, which is just below the peak in $R_{12;34}$ at 180 K (Fig. 3F). At the lowest temperature, σ_s is roughly five times larger than the bulk, which is remarkable for a bulk thickness of $t = 210$ μm.

The sample variation of the surface state is highlighted in the FEA of Corbino disk S2. The low-temperature bulk gap is comparable at $\Delta = 4.2$ meV, but σ_b continues to decrease with temperature (Fig. 3G). Likewise, σ_s keeps increasing below 120 K rather than reaching a temperature-independent value (Fig. 3H). Because of the large conductivity of the bulk, the ratio of $\sigma_b{}^* t/\sigma_s$ does not reach unity until 50 K (Fig. 3I). However, at base temperature, surface conductivity reaches 10 times that of the bulk.

DISCUSSION

Our discovery of a metallic surface state in $U_3Bi_4Ni_3$ is particularly important because, to our knowledge, it is one of only a few examples of such a state in Kondo insulators, with similar behavior observed in both SmB_6 and YbB_{12}. All three materials exhibit similar electron transport characteristics: activated behavior at high temperatures and resistivity saturation at low temperatures, although the bulk resistivity of SmB_6 is a few orders of magnitude higher than that of $U_3Bi_4Ni_3$ (*61*, *62*). What makes $U_3Bi_4Ni_3$ more intriguing is that its surface state emerges at a much higher temperature. The similarities and differences between $U_3Bi_4Ni_3$ and these well-studied Kondo insulators may shed light on the mechanisms underlying metallic surface states in these materials.

One key similarity across these materials is the exceptional robustness of the surface state. In our study, surface-dominated transport has been universally observed across all samples and surfaces of $U_3Bi_4Ni_3$, suggesting that the surface state is exceptionally robust and unaffected by surface conditions and impurities, similar to SmB_6 (*61*, *62*). This robustness is further emphasized by the fact that the surface state of $U_3Bi_4Ni_3$ remains dominant over a wide temperature range, achieving conductivity levels one order of magnitude higher than the bulk, despite variations in bulk conductivity that may indicate the presence of impurity bands in the bulk. This resilience is notable, especially considering that the surfaces have been exposed to air and contaminants during the polishing process.

This behavior is reminiscent of SmB_6, where nonstoichiometrically grown samples exhibit flattening of inverted resistance at low temperatures due to bulk impurities (*61*). However, in both materials, the surface state remains dominant, indicating a level of resilience that is unusual for trivial surface states, which typically lack such robustness and may arise only under specific conditions. This resilience suggests that the surface states in $U_3Bi_4Ni_3$, like those in SmB_6, may be inherently protected. Among the known mechanisms for robust surface states, topological band inversion stands out as the most plausible origin for such persistent surface conductivity. However, because of Kondo hybridization, simple density functional theory + U calculations may not be able to capture the electronic structure of $U_3Bi_4Ni_3$ (see the Supplementary Materials). In addition, unlike SmB_6 and YbB_{12}, which have inversion symmetry and thus enable a straightforward determination of band topology at high-symmetry points without any detailed knowledge of the bands (*63*), $U_3Bi_4Ni_3$ lacks inversion symmetry. As a result, establishing its topological index requires a detailed understanding of the Bloch states throughout the entire Brillouin zone. This heightened sensitivity means that even minor inaccuracies in the calculated band structure can lead to incorrect conclusions about its topological nature. More advanced methods, such as dynamical mean-field theory, are needed to fully understand the topology of $U_3Bi_4Ni_3$.

Despite these similarities, there are notable differences in the energy scales at which these surface states emerge, when comparing $U_3Bi_4Ni_3$ with SmB_6 and YbB_{12}. In SmB_6, the onset of Kondo hybridization begins at 60 to 90 K, and the full coherence is established below 30 to 40 K (*47*, *48*). The surface state, emerging at 4 K, arises from the Kondo ground state (*64*, *65*). Similarly, YbB_{12} has a Kondo temperature of 200 K (*49*, *66*), but the resistivity saturation does not happens until below 2 K (*8*). In contrast, the surface state of $U_3Bi_4Ni_3$ appears above the Kondo temperature: The emergence of the surface state has a concrete temperature scale between 200 and 250 K, while the Kondo energy scale is set at around $T_K = 100$ K.

The observation of a surface state emerging at temperatures above the Kondo temperature raises important questions about the origin of the surface state in $U_3Bi_4Ni_3$. One possibility is that a robust, protected surface state already exists at high temperatures, potentially associated with a topological gap. Upon cooling through the Kondo temperature, the gap is renormalized and reduced in size, but the fundamental nature of the surface state remains unchanged. This interpretation is supported by the absence of gap closure throughout the entire temperature range, suggesting that the topology remains consistent through the Kondo coherence process, as a change in topology would typically require the closing and reopening of a gap. The dual-gap features observed in both standard and inverted resistance transport, as well as in the bulk conductivity revealed through FEA, are also consistent with the gap renormalization by the Kondo hybridization. In this scenario, there is a crossover between a topological insulator (TI) and a Kondo topological insulator (KTI), which are smoothly connected without any phase boundary. One phase containing both a TI region and a KTI region, and a adiabatic continuity between the two regions is an interesting theory conjecture that requires further investigated in the future. An important question is whether the Kondo mechanism can still operate within an insulating phase. In principle, Kondo physics relies on hybridization between conduction and localized electrons, which typically requires a well-defined Fermi surface. However, this apparent contradiction can be reconciled if we consider a strongly correlated insulating state. At high temperatures, strong localization mechanisms dominate, suppressing electron mobility. As the temperature decreases, electron coherence improves, allowing some electrons to become sufficiently delocalized to screen local moments. In this way, Kondo behavior can emerge even within an ostensibly insulating phase.

Alternatively, the surface state observed at high temperatures might not be due to a topological gap but instead arise from a trivial origin, only becoming protected as the material transitions into the Kondo insulator state upon cooling. Our data do not provide definitive answers to distinguish between the two, and further investigation is needed to determine which mechanism—or combination of mechanisms—best explains the metallic surface state in $U_3Bi_4Ni_3$. Regardless, this behavior highlights the intricate relationship between Kondo physics and surface states, making $U_3Bi_4Ni_3$ an important system for understanding the fundamental physics governing metallic surface states in strongly correlated materials.

Regardless of their precise nature, the surface states observed in $U_3Bi_4Ni_3$ present an example of a robust, two-dimesional (2D) electron gas system. The interplay of Kondo physics within these 2D surface states introduces strong electron correlations and pronounced spin-orbit coupling, which is anticipated to exceed that of other well-studied 2D gases, such as semiconductor interfaces, graphene, and transition metal dichalcogenides. Moreover, these surface states

exhibit high conductivity and mobility, with sheet conductivity at 5 K reaching 0.1 to 0.5 ohm^{-1}, an order of magnitude higher than that of SmB_6 (0.02 ohm^{-1}) (*61*) and FeSi (0.01 ohm^{-1}) (*62*) and comparable to Bi_2Se_3 (*67*). The unique combination of strong correlations, enhanced spin-orbit coupling, and high mobility in this 2D system makes the surface states of $U_3Bi_4Ni_3$ particularly worthy of further investigation, as they could provide valuable insights into the complex interplay of these ingredients and potentially lead to the discovery of emergent quantum phenomena.

Our transport measurements and FEA analysis establish $U_3Bi_4Ni_3$ as a Kondo insulator with a robust metallic surface state, one of the only known examples besides SmB_6 and YbB_{12}. Notably, the surface state in $U_3Bi_4Ni_3$ emerges at a much higher temperature, above the Kondo temperature, which calls for further investigation to understand the origin of this phenomenon. This distinction may provide insights into the mechanism behind the surface states in Kondo insulators. Furthermore, the unique combination of high conductivity, mobility, and strong correlations observed in this system may give rise to emergent quantum phenomena, highlighting its importance for deepening our understanding of strongly correlated surface states in Kondo insulators.

METHODS

Sample synthesis

Single crystals of $U_3Bi_4Ni_3$ were prepared using the molten metal Flux method, with Bi as the solvent. Following the reported procedure (*43*), the raw elements were prepared in molar ratios of U:Bi:Ni = 1:10:2 and placed into an alumina crucible, which was sealed in a quartz tube with argon gas at 0.265 atm. The furnace was heated to 1150°C and then cooled to a temperature of 650°C at 5°C/hour. To separate the crystals from the Bi Flux,the quartz tube was then taken out of the furnace at 650°C and quickly inverted and placed into a centrifuge for 10 s. The $U_3Bi_4Ni_3$ single crystals were confirmed with powder x-ray diffraction (Cu-K_α) with a Rigaku MiniFlex. Energy-dispersive x-ray spectroscopy measurements were performed using a Thermo Fisher Scientific Quattro environmental scanning electron microscope.

Sample preparation and measurement

The samples prepared for resistivity measurements by polishing to a thickness of 100 to 200 μm and Pt wire were attached using silver epoxy. A Hall bar is prepared with a standard four-wire measurement, through a pair of Hall contacts inserted between the voltage leads. The Corbino disk geometry is prepared by drawing a ring of photoresist on the sample face and around the sample edge, to prevent from shorting the top and bottom surfaces. A gold sputter deposition of 50 nm forms an inner and outer electrode. This process is repeated on the bottom surface, to form another pair of electrodes. Electronic transport, specific heat, and magnetization measurements were performed in the Quantum Design Physical Property Measurement System using the resistivity, specific heat, and vibrating sample magnetometer options.

Finite element analysis

We studied the dependence of $R_{12;12}$ and $R_{12;34}$ on the bulk to surface conductivity ratio by performing FEA using the COMSOL MULTIPHYSICS AC/DC module. We used electric currents and electric currents in layered shells interfaces of the AC/DC module to build the bulk and surface conducting channels, respectively. We used the same dimensions as the experimental samples in our simulation. In COMSOL, we can measure the value of $R_{12;12}$ and $R_{12;34}$ for a specific value of the bulk to surface conductivity ratio $\left(\frac{\sigma_b t}{\sigma_s}\right)$ used in simulation. By varying the bulk to surface conductivity ratios used in the simulation, we get two curves: $R^s_{12;12}\left(\frac{\sigma_b t}{\sigma_s}\right)$ and $R^s_{12;34}\left(\frac{\sigma_b t}{\sigma_s}\right)$, where the superscript "s" represent simulation. On the other hand, we obtained $R^e_{12;12}(T)$ and $R^e_{12;34}(T)$ from experiment measurement, where the superscript "e" represent experiment. We fit the $\frac{R^s_{12;12}}{R^s_{12;34}}\left(\frac{\sigma_b t}{\sigma_s}\right)$ from simulation and $\frac{R^e_{12;12}}{R^e_{12;34}}(T)$ from experiment to get $\frac{\sigma_b t}{\sigma_s}(T)$, which is shown in Fig. 3 (F and I). Because in simulation we know the value of σ_s used, we also have the curve of $R^s_{12;12}\sigma_s\left(\frac{\sigma_b t}{\sigma_s}\right)$. Plugging in $\frac{\sigma_b t}{\sigma_s}(T)$, we get $R^s_{12;12}\sigma_s(T)$. Then assume $R^s_{12;12} = R^e_{12;12}$ and plug in $R^e_{12;12}(T)$, we get $\sigma_s(T)$, which is shown in Fig. 3 (E and H). In principle, we can also get $\sigma_s(T)$ using $R^s_{12;34}\sigma_s\left(\frac{\sigma_b t}{\sigma_s}\right)$. Both ways gave the same $\sigma_s(T)$, which we verified numerically. Plugging in $\sigma_s(T)$ to $\frac{\sigma_b t}{\sigma_s}(T)$, we get $\sigma_b(T)$, which are shown in Fig. 3 (D and G).

ARPES measurement

ARPES measurements were performed at beamline I05 of the Diamond Light Source. The angle resolution was ≤0.2°, and the overall energy resolution was set ≤25 meV. The 98- and 92-eV photon energy were used to examine the difference between measurements performed on- and off-resonance at the uranium O edge. The fresh surfaces for ARPES measurement were obtained by cleaving the samples in situ in the measurement chamber. During the measurements, the chamber pressure was kept below 2×10^{-10} mbar, and the sample temperature was 6 K.

Density functional theory

Electronic structures are calculated with the density functional theory as implemented in the Vienna Ab initio Simulation Package (*68*), combining the Perdew-Burke-Ernzerhof–type generalized gradient approximation (*69*) for the exchange-correlation interaction between electrons. The experimental crystal structure is used. A cutoff energy for the plane-wave basis set is 350 eV. The k-mesh grid for the Brillouin zone is 8 × 8 × 8. The Hubbard U correction for both the Ni d (Ud = 0, 2, and 4 eV) and U f (Uf = 0, 2, 4, and 6 eV) orbitals is used. Spin-orbital coupling is included throughout. The wannier90 software (*70*) interface is used to obtain the Wannier Hamiltonian for Wannier charge center calculations.

Supplementary Materials

This PDF file includes:

Supplementary Text
Table S1
Figs. S1 to S8

REFERENCES AND NOTES

1. H. Tsunetsugu, M. Sigrist, K. Ueda, The ground-state phase diagram of the one-dimensional Kondo lattice model. *Rev. Mod. Phys.* **69**, 809–864 (1997).
2. R. Jullien, J. N. Fields, S. Doniach, Zero-temperature real-space renormalization-group method for a Kondo-lattice model hamiltonian. *Phys. Rev. B* **16**, 4889–4900 (1977).
3. C. Lacroix, M. Cyrot, Phase diagram of the Kondo lattice. *Phys. Rev. B* **20**, 1969–1976 (1979).

4. N. Read, D. M. Newns, S. Doniach, Stability of the Kondo lattice in the large-*N* limit. *Phys. Rev. B.* **30**, 3841 (1984).
5. H. Kaga, H. Kubo, T. Fujiwara, Coherent Kondo-lattice state and the crossover transitions in the Anderson-lattice model. *Phys. Rev. B* **37**, 341–355 (1988).
6. P. Kumar, N. S. Vidhyadhiraja, From mixed valence to the Kondo lattice regime. *J. Phys. Condens. Matter* **23**, 485601 (2011).
7. W. A. Phelan, S. M. Koohpayeh, P. Cottingham, J. W. Freeland, J. C. Leiner, C. L. Broholm, T. M. McQueen, Correlation between bulk thermodynamic measurements and the low-temperature-resistance plateau in SmB_6. *Phys. Rev. X.* **4**, 031012 (2014).
8. Y. Sato, Z. Xiang, Y. Kasahara, S. Kasahara, L. Chen, C. Tinsman, F. Iga, J. Singleton, N. L. Nair, N. Maksimovic, et al., Topological surface conduction in Kondo insulator YbB_{12}. *J. Phys. D Appl. Phys.* **54**, 404002 (2021).
9. L. Li, K. Sun, C. Kurdak, J. Allen, Emergent mystery in the Kondo insulator samarium hexaboride. *Nat. Rev. Phys.* **2**, 463–479 (2020).
10. J. C. Nickerson, R. M. White, K. N. Lee, R. Bachmann, T. H. Geballe, G. W. Hull Jr., Physical properties of Smb_6. *Phys. Rev. B* **3**, 2030–2042 (1971).
11. P. S. Riseborough, Collapse of the coherence gap in Kondo semiconductors. *Phys. Rev. B.* **68**, 235213 (2003).
12. I. Batko, M. Batkova, SmB_6: Topological insulator or semiconductor with valence-fluctuation induced hopping transport? *Solid State Commun.* **196**, 18–23 (2014).
13. T. Takimoto, SmB_6: A promising candidate for a topological insulator. *J. Physical Soc. Japan* **80**, 123710 (2011).
14. F. Lu, J. Zhao, H. Weng, Z. Fang, X. Dai, Correlated topological insulators with mixed valence. *Phys. Rev. Lett.* **110**, 096401 (2013).
15. J. Kim, K. Kim, C.-J. Kang, S. Kim, H. C. Choi, J.-S. Kang, J. D. Denlinger, B. I. Min, Termination dependent surface in-gap states in a potential mixed-valent topological insulator: SmB_6. *Phys. Rev. B.* **90**, 075131 (2014).
16. P. Thunström, K. Held, Topology of SmB_6 determined by dynamical mean field theory. *Phys. Rev. B.* **104**, 075131 (2021).
17. L. Fu, Topological crystalline insulators. *Phys. Rev. Lett.* **106**, 106802 (2011).
18. H. Weng, J. Zhao, Z. Wang, Z. Fang, X. Dai, Topological crystalline Kondo insulator in mixed valence ytterbium borides. *Phys. Rev. Lett.* **112**, 016403 (2014).
19. Z.-H. Zhu, A. Nicolaou, G. Levy, N. P. Butch, P. Syers, X. F. Wang, J. Paglione, G. A. Sawatzky, I. S. Elfimov, A. Damascelli, Polarity-driven surface metallicity in SmB_6. *Phys. Rev. Lett.* **111**, 216402 (2013).
20. K. Hagiwara, Y. Ohtsubo, M. Matsunami, S.-i. Ideta, K. Tanaka, H. Miyazaki, J. E. Rault, P. L. Fèvre, F. Bertran, A. Taleb-Ibrahimi, R. Yukawa, M. Kobayashi, K. Horiba, H. Kumigashira, K. Sumida, T. Okuda, F. Iga, S.-i. Kimura, Surface Kondo effect and non-trivial metallic state of the Kondo insulator YbB_{12}. *Nat. Commun.* **7**, 12690 (2016).
21. V. B. Zabolotnyy, K. Fürsich, R. J. Green, P. Lutz, K. Treiber, C.-H. Min, A. V. Dukhnenko, N. Y. Shitsevalova, V. B. Filipov, B. Y. Kang, B. K. Cho, R. Sutarto, F. He, F. Reinert, D. S. Inosov, V. Hinkov, Chemical and valence reconstruction at the surface of SmB_6 revealed by means of resonant soft x-ray reflectometry. *Phys. Rev. B.* **97**, 205416 (2018).
22. P. Hlawenka, K. Siemensmeyer, E. Weschke, A. Varykhalov, J. Sánchez-Barriga, N. Y. Shitsevalova, A. V. Dukhnenko, V. B. Filipov, S. Gabáni, K. Flachbart, O. Rader, E. D. L. Rienks, Samarium hexaboride is a trivial surface conductor. *Nat. Commun.* **9**, 517 (2018).
23. B. S. Tan, Y.-T. Hsu, B. Zeng, M. Ciomaga Hatnean, N. Harrison, Z. Zhu, M. Hartstein, M. Kiourlappou, A. Srivastava, M. D. Johannes, T. P. Murphy, J.-H. Park, L. Balicas, G. G. Lonzarich, G. Balakrishnan, S. E. Sebastian, Unconventional fermi surface in an insulating state. *Science* **349**, 287–290 (2015).
24. M. Hartstein, W. H. Toews, Y.-T. Hsu, B. Zeng, X. Chen, M. Ciomaga Hatnean, Q. R. Zhang, S. Nakamura, A. S. Padgett, G. Rodway-Gant, J. Berk, M. K. Kingston, G. H. Zhang, M. K. Chan, S. Yamashita, T. Sakakibara, Y. Takano, J.-H. Park, L. Balicas, N. Harrison, N. Shitsevalova, G. Balakrishnan, G. G. Lonzarich, R. W. Hill, M. Sutherland, S. E. Sebastian, Fermi surface in the absence of a fermi liquid in the Kondo insulator SmB_6. *Nat. Phys.* **14**, 166–172 (2017).
25. P. G. LaBarre, A. Rydh, J. Palmer-Fortune, J. Frothingham, S. Hannahs, A. P. Ramirez, N. A. Fortune, Magnetoquantum oscillations in the specific heat of a topological Kondo insulator. *J. Phys. Condens. Matter* **34**, 36LT01 (2022).
26. Z. Xiang, Y. Kasahara, T. Asaba, B. Lawson, C. Tinsman, L. Chen, K. Sugimoto, S. Kawaguchi, Y. Sato, G. Li, S. Yao, Y. L. Chen, F. Iga, J. Singleton, Y. Matsuda, L. Li, Quantum oscillations of electrical resistivity in an insulator. *Science* **362**, 65–69 (2018).
27. Y. Sato, Z. Xiang, Y. Kasahara, T. Taniguchi, S. Kasahara, L. Chen, T. Asaba, C. Tinsman, H. Murayama, O. Tanaka, Y. Mizukami, T. Shibauchi, F. Iga, J. Singleton, L. Li, Y. Matsuda, Unconventional thermal metallic state of charge-neutral fermions in an insulator. *Nat. Phys.* **15**, 954–959 (2019).
28. Z. Xiang, L. Chen, K.-W. Chen, C. Tinsman, Y. Sato, T. Asaba, H. Lu, Y. Kasahara, M. Jaime, F. Balakirev, F. Iga, Y. Matsuda, J. Singleton, L. Li, Unusual high-field metal in a Kondo insulator. *Nat. Phys.* **17**, 788–793 (2021).
29. Z. Xiang, K.-W. Chen, L. Chen, T. Asaba, Y. Sato, N. Zhang, D. Zhang, Y. Kasahara, F. Iga, W. A. Coniglio, Y. Matsuda, J. Singleton, L. Li, Hall anomaly, quantum oscillations and possible lifshitz transitions in Kondo insulator YbB_{12}: Evidence for unconventional charge transport. *Phys. Rev. X.* **12**, 021050 (2022).
30. C. A. Mizzi, S. K. Kushwaha, P. F. Rosa, W. A. Phelan, D. C. Arellano, L. A. Pressley, T. M. McQueen, M. K. Chan, N. Harrison, The reverse quantum limit and its implications for unconventional quantum oscillations in YbB_{12}. *Nat. Commun.* **15**, 1607 (2024).
31. D. Chowdhury, I. Sodemann, T. Senthil, Mixed-valence insulators with neutral fermi surfaces. *Nat. Commun.* **9**, 1766 (2018).
32. G. Baskaran, Majorana fermi sea in insulating SmB_6: A proposal and a theory of quantum oscillations in Kondo insulators. arXiv:1507.03477 [cond-mat.str-el] (2015).
33. O. Erten, P.-Y. Chang, P. Coleman, A. M. Tsvelik, Skyrme insulators: Insulators at the brink of superconductivity. *Phys. Rev. Lett.* **119**, 057603 (2017).
34. P. Coleman, E. Miranda, A. Tsvelik, Are Kondo insulators gapless? *Physica B Condens. Matter* **186-188**, 362–364 (1993).
35. P. Coleman, E. Miranda, A. Tsvelik, Odd-frequency pairing in the Kondo lattice. *Phys. Rev. B* **49**, 8955–8982 (1994).
36. P. Coleman, L. B. Ioffe, A. M. Tsvelik, Simple formulation of the two-channel Kondo model. *Phys. Rev. B* **52**, 6611–6627 (1995).
37. T. Senthil, S. Sachdev, M. Vojta, Fractionalized fermi liquids. *Phys. Rev. Lett.* **90**, 216403 (2003).
38. T. Yoshida, R. Peters, N. Kawakami, Non-hermitian perspective of the band structure in heavy-fermion systems. *Phys. Rev. B.* **98**, 035141 (2018).
39. Y. Nagai, Y. Qi, H. Isobe, V. Kozii, L. Fu, DMFT reveals the non-hermitian topology and Fermi arcs in heavy-fermion systems. *Phys. Rev. Lett.* **125**, 227204 (2020).
40. J. Smith, E. Kmetko, Magnetism or bonding: A nearly periodic table of transition elements. *J. Less Common Met.* **90**, 83–88 (1983).
41. T. Endstra, G. J. Nieuwenhuys, J. A. Mydosh, Hybridization model for the magnetic-ordering behavior of uranium- and cerium-based 1:2:2 intermetallic compounds. *Phys. Rev. B Condens. Matter* **48**, 9595–9605 (1993).
42. Q. G. Sheng, B. R. Cooper, S. P. Lim, First-principle study of hybridization effects and magnetic ordering in correlated-electron uranium systems. *Phys. Rev. B Condens. Matter* **50**, 9215–9225 (1994).
43. T. Klimczuk, H.-o. Lee, F. Ronning, T. Durakiewicz, N. Kurita, H. Volz, E. D. Bauer, T. McQueen, R. Movshovich, R. J. Cava, J. D. Thompson, Physical properties of the uranium ternary compounds $U_3Bi_4M_3$ (M = Ni,Rh). *Phys. Rev. B.* **77**, 245111 (2008).
44. S.-H. Baek, N. J. Curro, T. Klimczuk, H. Sakai, E. D. Bauer, F. Ronning, J. D. Thompson, Hybridization driven gap in $U_3Bi_4Ni_3$: A 209Bi NMR/NQR study. *Phys. Rev. B.* **79**, 195120 (2009).
45. B. Gorshunov, N. Sluchanko, A. Volkov, M. Dressel, G. Knebel, A. Loidl, S. Kunii, Low-energy electro dynamics of SmB_6. *Phys. Rev. B.* **59**, 1808 (1999).
46. J. Yamaguchi, A. Sekiyama, M. Y. Kimura, H. Sugiyama, Y. Tomida, G. Funabashi, S. Komori, T. Balashov, W. Wulfhekel, T. Ito, S. Kimura, A. Higashiya, K. Tamasaku, M. Yabashi, T. Ishikawa, S. Yeo, S.-I. Lee, F. Iga, T. Takabatake, S. Suga, Different evolution of the intrinsic gap in strongly correlated SmB_6 in contrast to YbB_{12}. *New J. Phys.* **15**, 043042 (2013).
47. X. Zhang, N. P. Butch, P. Syers, S. Ziemak, R. L. Greene, J. Paglione, Hybridization, inter-ion correlation, and surface states in the Kondo insulator SmB_6. *Phys. Rev. X.* **3**, 011011 (2013).
48. W. Ruan, C. Ye, M. Guo, F. Chen, X. Chen, G.-M. Zhang, Y. Wang, Emergence of a coherent in-gap state in the SmB_6 Kondo insulator revealed by scanning tunneling spectroscopy. *Phys. Rev. Lett.* **112**, 136401 (2014).
49. Y. Takeda, M. Arita, M. Higashiguchi, K. Shimada, H. Namatame, M. Taniguchi, F. Iga, T. Takabatake, High-resolution photoemission study of the temperature-dependent c–f hybridization gap in the Kondo semiconductor YbB_{12}. *Phys. Rev. B.* **73**, 033202 (2006).
50. N. Nagaosa, J. Sinova, S. Onoda, A. H. MacDonald, N. P. Ong, Anomalous Hall effect. *Rev. Mod. Phys.* **82**, 1539–1592 (2010).
51. N. W. Ashcroft, N. D. Mermin, *Solid State Physics* (Cengage Learning, 2022).
52. P. M. Levy, Extraordinary Hall effect in Kondo-type systems: Contributions from anomalous velocity. *Phys. Rev. B Condens. Matter* **38**, 6779–6797 (1988).
53. A. Fert, A. Friederich, A. Hamzic, Hall effect in dilute magnetic alloys. *J. Magn. Magn. Mater.* **24**, 231–257 (1981).
54. J. Kondo, Effect of ordinary scattering on exchange scattering from magnetic impurity in metals. *Phys. Rev.* **169**, 437–440 (1968).
55. K. Nagaoka, T. Jamneala, M. Grobis, M. F. Crommie, Temperature dependence of a single Kondo impurity. *Phys. Rev. Lett.* **88**, 077205 (2002).
56. Q. Y. Chen, X. B. Luo, D. H. Xie, M. L. Li, X. Y. Ji, R. Zhou, Y. B. Huang, W. Zhang, W. Feng, Y. Zhang, L. Huang, Q. Q. Hao, Q. Liu, X. G. Zhu, Y. Liu, P. Zhang, X. C. Lai, Q. Si, S. Y. Tan, Orbital-selective Kondo entanglement and antiferromagnetic order in USb_2. *Phys. Rev. Lett.* **123**, 106402 (2019).
57. H. Siddiquee, C. Broyles, E. Kotta, S. Liu, S. Peng, T. Kong, B. Kang, Q. Zhu, Y. Lee, L. Ke, H. Weng, J. D. Denlinger, L. A. Wray, S. Ran, Breakdown of the scaling relation of anomalous Hall effect in Kondo lattice ferromagnet USbTe. *Nat. Commun.* **14**, 527 (2023).
58. M. Neupane, N. Alidoust, S.-Y. Xu, T. Kondo, Y. Ishida, D. J. Kim, C. Liu, I. Belopolski, Y. J. Jo, T.-R. Chang, H.-T. Jeng, T. Durakiewicz, L. Balicas, H. Lin, A. Bansil, S. Shin, Z. Fisk,

M. Z. Hasan, Surface electronic structure of the topological Kondo-insulator candidate correlated electron system SmB_6. *Nat. Commun.* **4**, 2991 (2013).
59. J. Jiang, S. Li, T. Zhang, Z. Sun, F. Chen, Z. R. Ye, M. Xu, Q. Q. Ge, S. Y. Tan, X. H. Niu, M. Xia, B. P. Xie, Y. F. Li, X. H. Chen, H. H. Wen, D. L. Feng, Observation of possible topological in-gap surface states in the Kondo insulator SmB_6 by photoemission. *Nat. Commun.* **4**, 3010 (2013).
60. Y. S. Eo, K. Sun, i. m. c. Kurdak, D.-J. Kim, Z. Fisk, Inverted resistance measurements as a method for characterizing the bulk and surface conductivities of three-dimensional topological insulators. *Phys. Rev. Appl.* **9**, 044006 (2018).
61. Y. S. Eo, A. Rakoski, J. Lucien, D. Mihaliov, Ç. Kurdak, P. F. Rosa, Z. Fisk, Transport gap in SmB_6 protected against disorder. *Proc. Natl. Acad. Sci. U.S.A.* **116**, 12638–12641 (2019).
62. Y. S. Eo, K. Avers, J. A. Horn, H. Yoon, S. R. Saha, A. Suarez, M. S. Fuhrer, J. Paglione, Extraordinary bulk-insulating behavior in the strongly correlated materials FeSi and $FeSb_2$. *Appl. Phys. Lett.* **122**, 233102 (2023).
63. M. Dzero, K. Sun, V. Galitski, P. Coleman, Topological kondo insulators. *Phys. Rev. Lett.* **104**, 106408 (2010).
64. D.-J. Kim, J. Xia, Z. Fisk, Topological surface state in the Kondo insulator samarium hexaboride. *Nat. Mater.* **13**, 466–470 (2014).
65. J. Yong, Y. Jiang, D. Usanmaz, S. Curtarolo, X. Zhang, L. Li, X. Pan, J. Shin, I. Takeuchi, R. L. Greene, Robust topological surface state in Kondo insulator SmB_6 thin films. *Appl. Phys. Lett.* **105**, 222403 (2014).
66. T. Susaki, A. Sekiyama, K. Kobayashi, T. Mizokawa, A. Fujimori, M. Tsunekawa, T. Muro, T. Matsushita, S. Suga, H. Ishii, T. Hanyu, A. Kimura, H. Namatame, M. Taniguchi, T. Miyahara, F. Iga, M. Kasaya, H. Harima, Low-energy electronic structure of the Kondo insulator YbB_{12}. *Phys. Rev. Lett.* **77**, 4269–4272 (1996).
67. Y. S. Kim, M. Brahlek, N. Bansal, E. Edrey, G. A. Kapilevich, K. Iida, M. Tanimura, Y. Horibe, S.-W. Cheong, S. Oh, Thickness-dependent bulk properties and weak antilocalization effect in topological insulator Bi_2Se_3. *Phys. Rev. B.* **84**, 073109 (2011).
68. G. Kresse, J. Furthmüller, Efficient iterative schemes for ab initio total-energy calculations using a plane-wave basis set. *Phys. Rev. B. Condens. Matter* **54**, 11169–11186 (1996).
69. J. P. Perdew, K. Burke, M. Ernzerhof, Generalized gradient approximation made simple. *Phys. Rev. Lett.* **77**, 3865–3868 (1996).
70. G. Pizzi, V. Vitale, R. Arita, S. Blügel, F. Freimuth, G. Géranton, M. Gibertini, D. Gresch, C. Johnson, T. Koretsune, J. Ibañez-Azpiroz, H. Lee, J. M. Lihm, D. Marchand, A. Marrazzo, Y. Mokrousov, J. I. Mustafa, Y. Nohara, Y. Nomura, L. Paulatto, S. Poncé, T. Ponweiser, J. Qiao, F. Thöle, S. S. Tsirkin, M. Wierzbowska, N. Marzari, D. Vanderbilt, I. Souza, A. A. Mostofi, J. R. Yates, Wannier90 as a community code: New features and applications. *J. Phys. Condens. Matter* **32**, 165902 (2020).

Acknowledgments: We acknowledge helpful discussions with Q. Si. **Funding:** Research at Washington University was supported by the National Science Foundation (NSF) Division of Materials Research Award DMR-2236528. C.B. acknowledges the NRT LinQ, supported by the NSF under grant no. 2152221. Research at University of Michigan was supported by the Air Force Office of Scientific Research through the Multidisciplinary University Research Initiative, award no. FA9550-23-1-0334 (X.W. and K.S.) and the Office of Naval Research through the Multidisciplinary University Research Initiative, award no. N00014-20-1-2479 (W.C. and K.S.). B.Y. acknowledges the financial support by the European Research Council (ERC Consolidator Grant "NonlinearTopo," no. 815869) and the ISF–Personal Research Grant (no. 2932/21) and the DFG (CRC 183, A02). Y.C. acknowledges the support from the National Natural Science Foundation of China (no. U23A6002). We acknowledge Diamond Light Source for time on Beamline I05 under proposal number SI36513. **Author contributions:** S.R., K.S., and B.Y. conceived and designed the study. C.B. synthesized the single crystalline samples of $U_3Bi_4Ni_3$. C.B. and H.S. performed the electrical transport and magnetic measurements. Q.X. fabricated devices using focused ion beam. X.W., W.C., W.L., Y.W., and K.S. performed the FEA. D.W. and Y.C. performed the ARPES measurement. H.T. and B.Y. performed the density functional theory calculations. S.L.G. performed the EDX measurements. Y.S.E., P.R., L.X., and R.C. performed the specific heat measurements. C.B. and S.R. wrote the manuscript with contributions from all authors. **Competing interests:** The authors declare that they have no competing interests. **Data and materials availability:** All data needed to evaluate the conclusions in the paper are present in the paper and/or the Supplementary Materials.

Submitted 10 June 2024
Accepted 14 February 2025
Published 21 March 2025
10.1126/sciadv.adq9952